



# The Nucleus of Interstellar Comet 2I/Borisov

David Jewitt<sup>1,2</sup>, Man-To Hui<sup>3</sup>, Yoonyoung Kim<sup>4</sup>, Max Mutchler<sup>5</sup>, Harold Weaver<sup>6</sup>, and Jessica Agarwal<sup>4</sup><sup>1</sup>Department of Earth, Planetary and Space Sciences, UCLA, Los Angeles, CA 90095-1567, USA; [jewitt@ucla.edu](mailto:jewitt@ucla.edu)<sup>2</sup>Department of Physics and Astronomy, UCLA, Los Angeles, CA 90095-1547, USA<sup>3</sup>Institute for Astronomy, University of Hawaii, Honolulu, HI 96822, USA<sup>4</sup>Max Planck Institute for Solar System Research, D-37077 Göttingen, Germany<sup>5</sup>Space Telescope Science Institute, Baltimore, MD 21218, USA<sup>6</sup>The Johns Hopkins University Applied Physics Laboratory, Laurel, MD 20723, USA

Received 2019 November 27; revised 2019 December 11; accepted 2019 December 14; published 2020 January 13

## Abstract

We present high-resolution imaging observations of interstellar comet 2I/Borisov (formerly C/2019 Q4) obtained using the *Hubble Space Telescope*. Scattering from the comet is dominated by a coma of large particles (characteristic size  $\sim 0.1$  mm) ejected anisotropically. Convolution modeling of the coma surface brightness profile sets a robust limit to the spherical-equivalent nucleus radius  $r_n \leq 0.5$  km (geometric albedo 0.04 assumed). We obtain an independent constraint based on the nongravitational acceleration of the nucleus, finding  $r_n > 0.2$  km (nucleus density  $\rho = 500$  kg m<sup>-3</sup> assumed). The profile and the nongravitational constraints cannot be simultaneously satisfied if  $\rho \leq 25$  kg m<sup>-3</sup>; the nucleus of comet Borisov cannot be a low-density fractal assemblage of the type proposed elsewhere for the nucleus of 1I/'Oumuamua. We show that the spin-up timescale to outgassing torques, even at the measured low production rates, is comparable to or shorter than the residence time in the Sun's water sublimation zone. The spin angular momentum of the nucleus should be changed significantly during the current solar flyby. Lastly, we find that the differential interstellar size distribution in the 0.5 mm to 100 m size range can be represented by power laws with indices  $< 4$  and that interstellar bodies of 100 m size scale strike Earth every one to two hundred million years.

*Unified Astronomy Thesaurus concepts:* Comets (280); Long period comets (933)

## 1. Introduction

Comet 2I/Borisov (hereafter simply “2I”) is the second interstellar interloper detected in the solar system (Borisov 2019), after 1I/'Oumuamua (“1I”). Scientific interest in these bodies lies in their role as the first known members of an entirely new population formed, presumably, by the ejection of planetesimals in the clearing phase of external protoplanetary disks (e.g., Moro-Martín 2018). Curiously, the first two interstellar objects appear physically quite different. Whereas 'Oumuamua was an apparently inactive, roughly 100 m scale body with a large amplitude lightcurve (Bannister et al. 2017; Jewitt et al. 2017; Meech et al. 2017; Drahus et al. 2018) 2I more closely resembles a typical solar system comet, with a prominent dust coma that was evident at discovery (Bolin et al. 2019; Guzik et al. 2019; Jewitt & Luu 2019) and weak spectral lines (Fitzsimmons et al. 2019; McKay et al. 2019) indicative of ongoing activity. Despite appearing inactive, comet 1I exhibited nongravitational acceleration (Micheli et al. 2018), likely caused by recoil forces from anisotropic mass loss (although other explanations have been advanced; Bialy & Loeb 2018; Flekkøy et al. 2019; Moro-Martín 2019).

Comet 2I passed perihelion on UT 2019 December 8 at distance  $q = 2.006$  au and will reach Jupiter's distance in 2020 July and Saturn's by 2021 March. Here, we present pre-perihelion *Hubble Space Telescope* (*HST*) observations at heliocentric distance  $r_H = 2.369$  au. A particular objective is to determine the effective size of the nucleus using the highest-resolution data.

## 2. Observations

All observations were obtained under the Director's Discretionary Time allocation GO 16009. We used the WFC3

charge-coupled device (CCD) camera on *HST*, which has pixels  $0''.04$  wide and gives a Nyquist-sampled resolution of about  $0''.08$  (corresponding to 160 km at the distance of 2I). In order to fit more exposures into the allocated time, only half of one of two WFC3 CCDs was read out, providing an  $80'' \times 80''$  field of view, with 2I approximately centrally located. The telescope was tracked at the instantaneous non-sidereal rate of the comet (up to about  $100''$  hr<sup>-1</sup>) and also dithered to mitigate the effects of bad pixels. All data were taken through the F350LP filter, which has a peak transmission  $\sim 28\%$ , an effective wavelength  $\lambda_e \sim 5846$  Å, and a FWHM  $\sim 4758$  Å. In each of the four orbits, we obtained six images each of 260 s duration. Geometric parameters of the observations are summarized in Table 1.

## 3. Discussion

*Morphology.* Figure 1 shows the appearance of 2I on UT 2019 October 12, in a composite image of 6240 s duration formed by aligning and combining all 24 images from the four *HST* orbits. Close to the nucleus, the coma shows a bi-lobed appearance reminiscent of the morphology observed in C/2014 B1 (Jewitt et al. 2019). There, it was attributed to low-latitude ejection of large (slow) dust particles from a nucleus rotating with its pole lying near the plane of the sky. We defer detailed modeling of the morphology of the dust coma pending the acquisition of additional images to be taken from a range of viewing perspectives. Such observations are already planned under GO 16009 and its continuation in GO 16041.

Comet 2I also shows an extensive tail of dust with an axis lying between the projected antisolar and negative heliocentric velocity vectors, marked in the figure by  $-\odot$  and  $-V$ , respectively. The tail extends to the edge of the WFC3 field of view, a distance at least  $40''$  from the nucleus in the

**Table 1**  
Observing Geometry

UT Date and Time	$\Delta T_p^a$	$r_H^b$	$\Delta^c$	$\alpha^d$	$\theta_\odot^e$	$\theta_{-V}^f$	$\delta_\oplus^g$
2019 Oct 12 13:44-20:42	-57	2.369	2.781	20.4	292.6	330.1	-13.7

**Notes.**

<sup>a</sup> Number of days from perihelion (UT 2019 December 8 = DOY 342). Negative numbers indicate pre-perihelion observations.

<sup>b</sup> Heliocentric distance, in au.

<sup>c</sup> Geocentric distance, in au.

<sup>d</sup> Phase angle, in degrees.

<sup>e</sup> Position angle of the projected antisolar direction, in degrees.

<sup>f</sup> Position angle of the projected negative heliocentric velocity vector, in degrees.

<sup>g</sup> Angle of Earth above the orbital plane, in degrees.

composite image, corresponding to a sky-plane distance  $\ell \gtrsim 8 \times 10^4$  km. The tail direction in Figure 1 allows us to make a simple estimate of the particle size by comparison with syndyne models, shown in Figure 2. The motion of cometary dust particles relative to their parent nucleus is controlled by the ratio of the force due to solar radiation pressure to the gravitational force, called  $\beta$ . Syndynes mark the locus of positions in the sky plane occupied by particles having a given  $\beta$  and emitted over a range of times. The figure shows syndynes for particles with  $\beta = 10^{-4}$ ,  $10^{-3}$ ,  $10^{-2}$ ,  $10^{-1}$ , and 1 ejected isotropically with zero initial relative velocity. For dielectric particles,  $\beta \sim a^{-1}$ , where  $a$  is the particle radius expressed in microns (Bohren & Huffman 1983). Figure 2 shows that the tail direction is best matched by  $\beta \sim 0.01$ , corresponding to particle radius  $a \sim 100 \mu\text{m}$  (consistent with Jewitt & Luu 2019). It is clear from the complexity of the coma, particularly in the central  $5''$ , that no single particle size model can fit the data, but we are confident that the particles are large and that micron-sized particles ( $\beta = 1$ ) alone cannot represent the comet. As on other comets, the paucity of small particles might be due to cohesive forces that selectively affect the escape under gas drag.

**Photometry.** The time dependence of the apparent magnitude of 2I is plotted in Figure 3, from measurements using a  $0''.2$  radius photometry aperture (400 km at the comet) with background subtraction from a contiguous aperture having an outer radius of  $0''.28$  (560 km). The measurements span a  $\sim 7$  hr interval, with a gap between UT 16 and 18 hr forced by technical issues with the telescope. A linear, least-squares fit to the data (gradient  $dV/dt = -0.001 \pm 0.002$  magnitudes  $\text{hr}^{-1}$ ), shown as a straight line in Figure 3, indicates no systematic trend in the apparent brightness on this timescale. However, the measured gradient is consistent with the 1%  $\text{day}^{-1}$  ( $4 \times 10^{-4}$  magnitudes  $\text{hr}^{-1}$ ) rate of brightening measured between September 13 and October 4 (Jewitt & Luu 2019). Deviations from the best fit, provide no definitive evidence for short-term variations and are consistent with the  $1\sigma = \pm 0.03$  magnitude statistical errors. We thus find no evidence for modulation of the light scattered from an 'Oumuamua-like rotating, aspherical nucleus. As we show below, the most likely explanation is coma dilution within the  $0''.2$  photometry aperture, because the cross-section of the nucleus is small compared to the combined cross-sections of the dust particles within the projected aperture.

**Crude Radius Estimate.** The best-fit value of the apparent magnitude from Figure 3 is  $V = 21.51 \pm 0.04$ . The absolute magnitude computed from  $V$  assuming a linear phase function of the form  $\Phi(\alpha) = 0.04$  magnitudes  $\text{degree}^{-1}$  is  $H = 16.60 \pm 0.04$  magnitudes, where the quoted uncertainty reflects only statistical fluctuations. Uncertainties in the phase function are systematic in nature and dominate the statistical errors. For example, plausible uncertainties in  $\Phi(\alpha)$  of  $\pm 0.02$  magnitudes  $\text{degree}^{-1}$  affect our best estimate of  $H$  by  $\pm 0.4$  magnitudes.

The scattering cross-section corresponding to  $H$ , in  $\text{km}^2$ , is calculated from

$$C_e = \frac{1.5 \times 10^6}{p_V} 10^{-0.4H}, \quad (1)$$

where  $p_V$  is the geometric albedo. The mean albedo of cometary nuclei is  $p_V \sim 0.04$  (Fernández et al. 2013) and, using this albedo, Equation (1) gives  $C_e = 8.6 \text{ km}^2$ . The radius of an equal-area circle is  $r_e = (C_e/\pi)^{1/2}$ , or  $r_e = 1.6$  km. This constitutes a crude but absolute upper limit to the radius of the nucleus, because the central  $0''.2$  aperture is strongly contaminated by dust.

**Radius from Profile Fitting.** To better remove the dust contamination of the near-nucleus region, we fitted a surface brightness model to the coma and extrapolated inward to the location of the nucleus, according to the prescription described in Hui & Li (2018). For this purpose, the surface brightness was fitted in  $1^\circ$  azimuthal segments over the radius range  $0''.24\text{--}1''.20$ . The weighted mean surface brightness within a set of nested annuli is shown in Figure 4. Statistical error bars, computed from the standard error on the mean of the value at each radius, are smaller than the plot symbols. Systematic errors, principally due to uncertainties in the background subtraction due to field objects and internal scattering, were found to be unimportant in the fitted region of the profile. Consistent profiles were obtained using data from the other three *HST* orbits and so these are not shown separately.

The fitted profiles were then convolved with the *HST* point-spread function provided by TinyTim (Krist et al. 2011), after adding a central point source signal to represent the nucleus. In the figure we show models in which the effective nucleus radii are  $r_n = 0, 0.3, 0.7,$  and  $1.0$  km, respectively (albedo  $p_V = 0.04$  assumed). By inspection of the figure, we conservatively set an empirical upper limit to the radius of the nucleus  $r_n \leq 0.5$  km, far smaller than the crude estimate given above and showing the importance of accurate dust subtraction.

**Other Radius Constraints.** Two other observations can be used to independently constrain the radius of the nucleus of 2I, although neither is as robust as the limit derived from the surface brightness profile. Both are based on knowledge of the mass production rate of 2I.

Cometary nongravitational motion provides a measure of the nucleus size, essentially because the sublimation rate is proportional to  $r_n^2$  while the mass is proportional to  $r_n^3$ . Small nuclei can be measurably accelerated by recoil forces from anisotropic sublimation while large nuclei cannot. The recoil force resulting from the loss of mass at rate  $\dot{M}$  and at speed  $V_{\text{th}}$  is  $F = f_{\text{ng}} \dot{M} V_{\text{th}}$ , where  $0 \leq f_{\text{ng}} \leq 1$  is a dimensionless number representing the degree of anisotropy of the mass loss. Isotropic emission, corresponding to zero net force on the nucleus, has



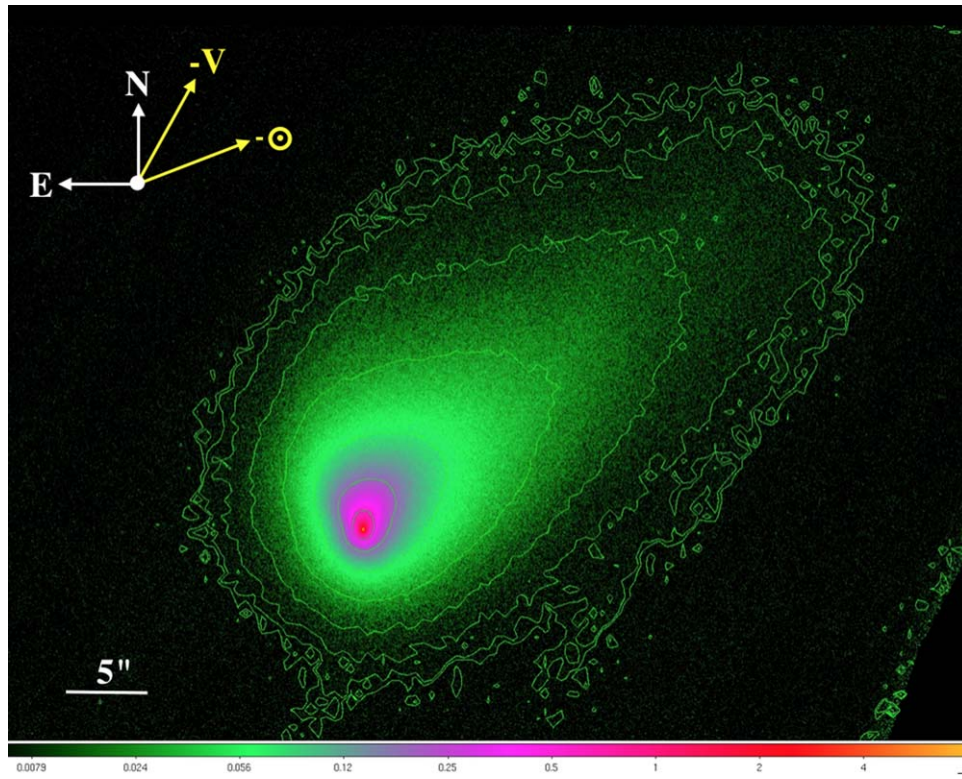


**Figure 1.** Composite WFC3 image of comet Borisov on UT 2019 October 12 with isophotal contours overlaid. The cardinal directions are marked, as are the projected antisolar vector ( $-\odot$ ) and the projected negative heliocentric velocity vector ( $-V$ ). A  $5''$  (10,000 km) scale bar is shown.

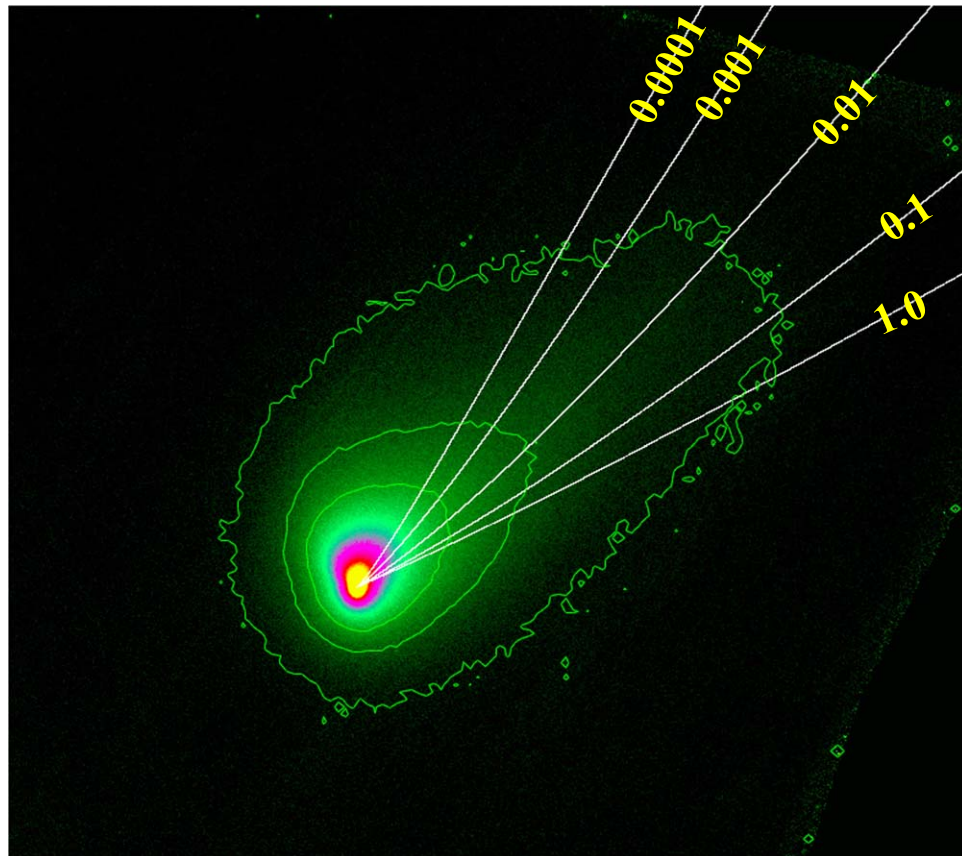


**Figure 2.** Comet Borisov on UT 2019 October 12 showing syndynes for particles with  $\beta = 10^{-4}$ ,  $10^{-3}$ ,  $10^{-2}$ ,  $10^{-1}$ , and 1, as marked. The axis of the tail is best represented by  $\beta = 0.01$ , corresponding to particle radius  $a \sim 100 \mu\text{m}$ . Direction arrows are the same as in Figure 1.

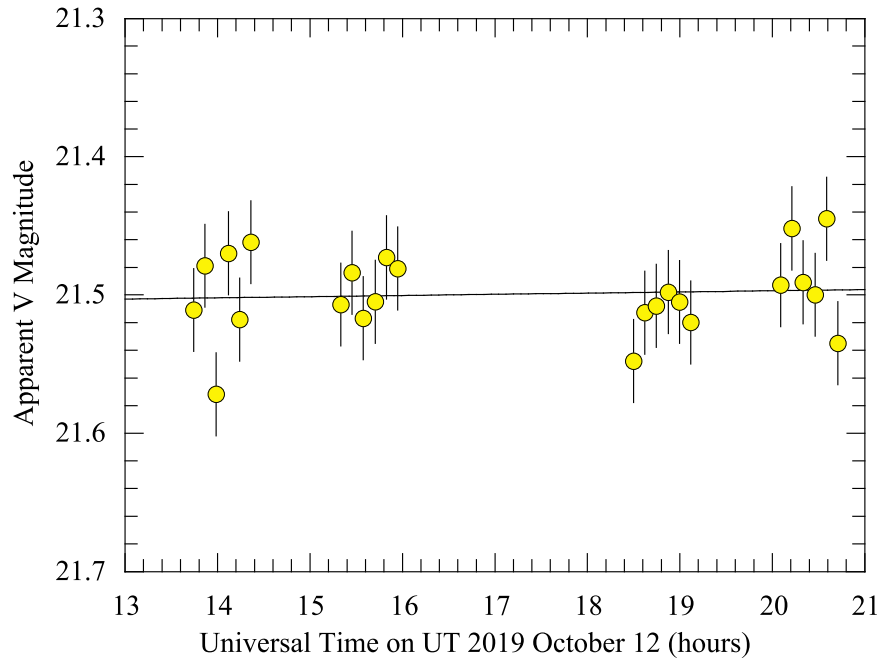


**Figure 3.** Apparent V magnitude within a  $0''.2$  radius photometry aperture on UT 2019 October 12. The straight line shows a linear, least-squares fit to the data with slope  $-0.001 \pm 0.002$  magnitudes  $\text{hr}^{-1}$ .

$f_{\text{ng}} = 0$ , while perfectly collimated emission has  $f_{\text{ng}} = 1$ . Observations show that sublimation-driven mass loss from comets is highly anisotropic, occurring primarily from the Sun-facing hemisphere. Through Newton’s law, we set  $F = 4\pi/3 \rho r_n^3 \mathcal{A}$ , where  $\mathcal{A}$  is the nongravitational acceleration [ $\text{m s}^{-2}$ ] of the nucleus. The effective radius of the nucleus is then given by

$$r_n = \left( \frac{3f_{\text{ng}} \dot{M} V_{\text{th}}}{4\pi\rho\mathcal{A}} \right)^{1/3}. \quad (2)$$

We use the mean thermal speed of molecules  $V_{\text{th}} = (8kT/(\pi\mu m_H))^{1/2}$ , where  $\mu = 18$  is the molecular weight of  $\text{H}_2\text{O}$ ,  $m_H = 1.67 \times 10^{-27}$  kg is the mass of the hydrogen atom, and  $T$  is the temperature of the sublimating surface, which we calculated from the equilibrium sublimation condition ( $T = 197$  K at 2 au). We find  $V_{\text{th}} = 480$   $\text{m s}^{-1}$ . The nucleus density was assumed to be  $\rho = 500$   $\text{kg m}^{-3}$  (Groussin et al. 2019).

The most direct estimates of the 2I mass-loss rate,  $\dot{M}$ , are provided by spectroscopic detections of the forbidden oxygen ([O I]6300 Å) line, which give  $Q_{\text{H}_2\text{O}} = (6.3 \pm 1.5) \times 10^{26}$  ( $\dot{M} = 20 \pm 5$   $\text{kg s}^{-1}$ ) at  $r_H = 2.38$  au (McKay et al. 2019). Less direct but broadly consistent estimates are provided by the resonant fluorescence band of CN3880 Å (Fitzsimmons et al. 2019). When scaled to OH rates using factors determined in solar system comets (A’Hearn et al. 1995), the CN detection gives water production rates  $Q_{\text{H}_2\text{O}} = (1.3\text{--}5.1) \times 10^{27}$   $\text{s}^{-1}$ , corresponding to  $40 \leq \dot{M} \leq 150$   $\text{kg s}^{-1}$  at  $r_H = 2.66$  au. Of these two measurements, we consider the one based on [O I] more likely to be accurate, given that the determination from CN is one additional step removed by the unmeasured OH/CN ratio.

Astrometric data provide a measure of  $\mathcal{A}$ , with the major limitation that, at the time of writing, the resulting deviations from purely gravitational orbit solutions are modest ( $1''$  to  $2''$ ), and the estimation of  $\mathcal{A}$  is therefore sensitive to astrometric

uncertainties as well as to the force model employed. The solutions are particularly sensitive to predisccovery observations reported by Ye et al. (2019), some of which appear questionable given the low signal-to-noise ratios in their data.

The most recent available orbit solution is JPL Horizons orbit#48 (dated 2019 December 9), which uses astrometry obtained between UT 2018 December 13 and 2019 December 4. The solution gives  $A1 = -9.1 \times 10^{-8}$ ,  $A2 = 2.3 \times 10^{-8}$ , and  $A3 = -1.2 \times 10^{-7}$ . Using the force model of Marsden et al. (1973), the derived acceleration of the nucleus is  $\mathcal{A} = 8 \times 10^{-7}$   $\text{m s}^{-2}$  at  $r_H = 2$  au. To check this, one of us (Man-To Hui) fitted a high quality subset of the astrometric data (enlarged to include astrometry up to 2019 December 8) to obtain  $A1 = (7.1 \pm 7.1) \times 10^{-8}$ ,  $A2 = (1.0 \pm 1.0) \times 10^{-7}$ , and  $A3 = (-1.6 \pm 1.9) \times 10^{-8}$ , where the quoted uncertainties are  $1\sigma$  standard deviations. In view of the errors, the fit indicates that the three components are not statistically different from zero. Therefore, we combined the measured values in quadrature to obtain a  $3\sigma$  limit to the acceleration at  $r_H = 2.00$  au,  $\mathcal{A} < 7 \times 10^{-7}$   $\text{m s}^{-2}$ . This is numerically close to the value obtained from JPL#48, but is interpreted as an upper limit to  $\mathcal{A}$  rather than a detection of it.

With  $\mathcal{A} < 7 \times 10^{-7}$   $\text{m s}^{-2}$ , nominal density  $\rho = 500$   $\text{kg m}^{-3}$  (Groussin et al. 2019), and  $f_{\text{ng}} = 1$ , Equation (2) gives  $r_n > 0.2$  km (point A in Figure 5). This value is consistent with  $r_n < 0.5$  km as obtained from the surface brightness profile and neatly brackets the nucleus radius,  $0.2 \leq r_n \leq 0.5$  km, provided  $\rho = 500$   $\text{kg m}^{-3}$ . However, since the density of 2I is unmeasured, we must also consider other values. In order to satisfy the profile constraint ( $r_n < 0.5$  km) while keeping  $\dot{M}$  and  $\mathcal{A}$  as measured, Equation (2) requires  $\rho > 25$   $\text{kg m}^{-3}$  (point B in Figure 5). This is interesting because much lower densities (e.g.,  $\rho = 10^{-2}$   $\text{kg m}^{-3}$ ) have been posited in fractal models of the nongravitational acceleration of the nucleus of 1I (Flekkøy et al. 2019; Moro-Martín 2019). Such low densities, when substituted into (Equation (2))

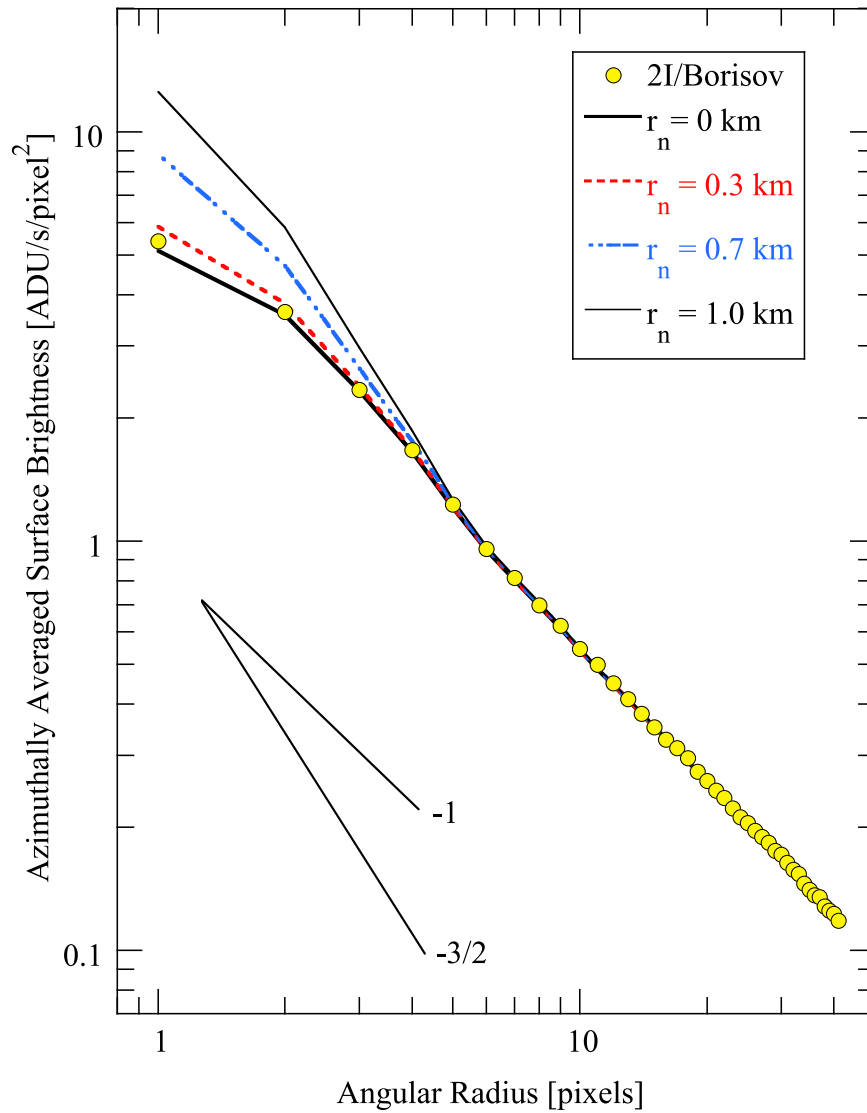


**Figure 4.** Surface brightness profile of comet Borisov (yellow circles) compared with models in which the nucleus radius (for assumed geometric albedo  $p_V = 0.04$ ) is  $r_n = 0$  km (thick black line), 0.3 km (dashed red line), 0.7 km (dashed-dotted blue line), and 1.0 km (thin black line). Lines in the lower left indicate logarithmic surface brightness gradients  $m = 1$  and  $m = -1.5$ , for comparison.

would give  $r_n > 7$  km, strongly violating the  $r_n < 0.5$  km limit obtained from the surface brightness profile (point C in Figure 5).

The third and weakest constraint on the nucleus radius is based on the production of gas. The rate of sublimation in equilibrium with sunlight is proportional to the sublimating area according to

$$r_n = \left( \frac{\dot{M}}{2\pi f_A f_s} \right)^{1/2}. \quad (3)$$

Here,  $f_A > 0$  is the active fraction of the Sun-facing hemisphere and  $f_s$  [ $\text{kg m}^{-2} \text{s}^{-1}$ ] is the specific rate of sublimation. We solved the equilibrium energy balance equation for water ice sublimation, neglecting conduction, assuming heating of the Sun-facing hemisphere of the nucleus. At  $r_H = 2.38$  au, the specific rate is  $f_s = 2 \times 10^{-5} \text{ kg m}^{-2} \text{ s}^{-1}$ , rising to  $f_s = 3 \times 10^{-5} \text{ kg m}^{-2} \text{ s}^{-1}$  at perihelion. Substituting active fraction  $f_A = 1$ , Equation (3) gives a nominal radius  $r_n = 0.4$  km, neatly falling between the bounds set by the profile and the nongravitational solutions (for  $\rho = 500 \text{ kg m}^{-3}$ ). However, the value of the active fraction,  $f_A$ , is not measured in 2I. In

well-measured solar system comets, this quantity is widely scattered from  $f_A \lesssim 10^{-2}$  to  $f_A \geq 1$ , with a tendency to be larger for smaller nuclei (A’Hearn et al. 1995). Values  $f_A < 1$  are possible if the nucleus is largely inert, allowing solutions with larger  $r_n$  by Equation (3). Values  $f_A \geq 1$  are possible when the measured gas is produced in part, or in all, by sublimation from grains in the coma (see Sekanina 2019), allowing solutions with smaller  $r_n$ . For these reasons, while noting the amazing concordance between estimates of the nucleus radius obtained from the three different methods, we consider the radius constraint from Equation (3) to be the weakest of the three presented here.

### 3.1. Spin-up, Size Distribution, and Impact Flux

The upper limit to the radius obtained using *HST* is an order of magnitude smaller than limits from ground-based data (e.g.,  $r_n \lesssim 7$  km; Ye et al. 2019). This small radius renders the nucleus of 2I susceptible to rapid changes in the spin state as a result of outgassing torques (Jewitt & Luu 2019). The e-folding

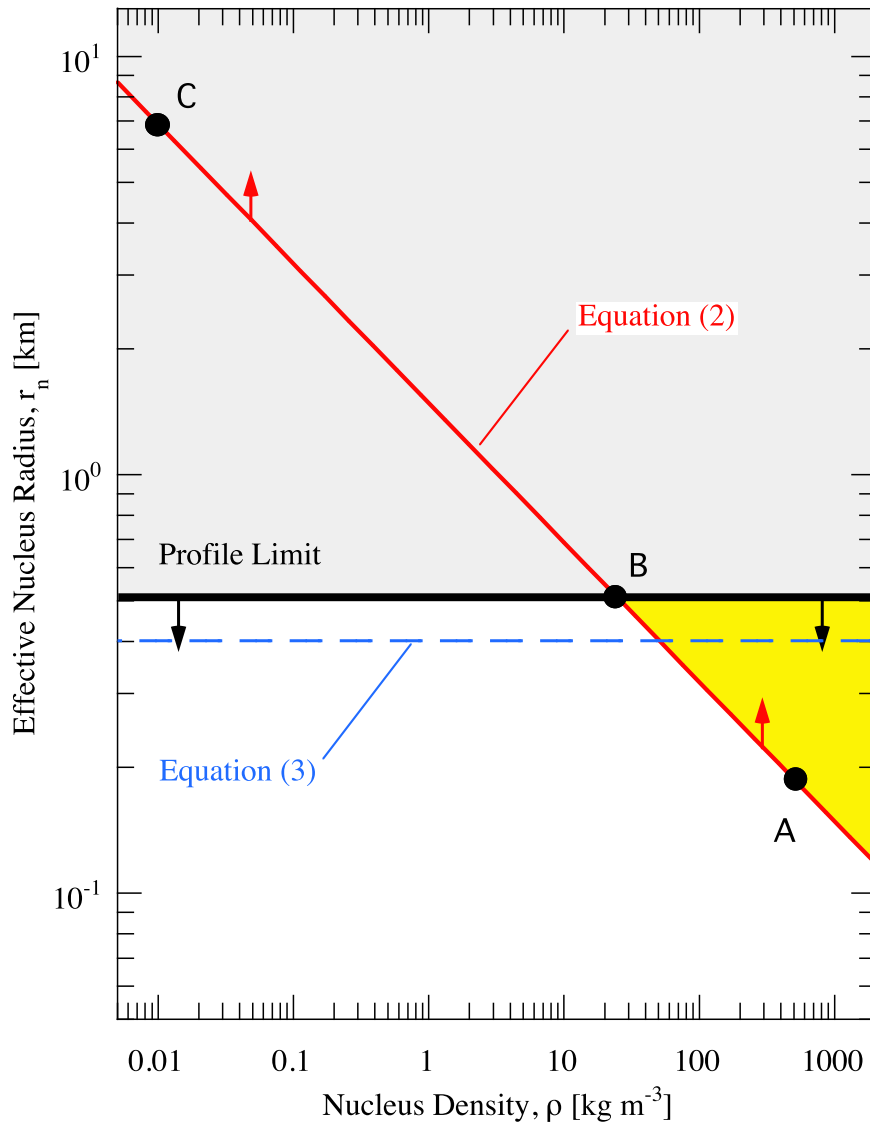


**Figure 5.** Radius ( $r_n$ ) vs. nucleus density ( $\rho$ ) plane for the nucleus of Comet Borisov. The upper limit from the fitted profile,  $r_n < 0.5$  km, is shown as a horizontal black line. The nongravitational motion lower limit (Equation (2)) is shown as a red line. Point A shows  $r_n > 0.2$  km, the radius limit inferred if the density is a comet-like  $\rho = 500 \text{ kg m}^{-3}$ . Solutions in the “sweet spot” yellow triangle satisfy both the profile and nongravitational constraints. No solutions exist for densities  $\rho < 25 \text{ kg m}^{-3}$  (point B). Very low (fractal) densities like that proposed for the nucleus of 1I/’Oumuamua (point C, with  $\rho = 10^{-2} \text{ kg m}^{-3}$ ) are specifically excluded. The blue dashed line shows Equation (3) computed with  $f_a = 1$ .

spin-up timescale for these torques is

$$\tau_s = \frac{\omega \rho r_n^4}{k_T V_{\text{th}} \dot{M}} \quad (4)$$

in which  $\omega = 2\pi/P$  is the angular frequency of the nucleus with rotation period  $P$ ,  $\rho$  is the nucleus bulk density,  $r_n$  its radius,  $V_{\text{th}}$  is the velocity of material leaving the nucleus, and  $\dot{M}$  is the rate of loss of mass (Jewitt 1997). The dimensionless moment arm lies in the range  $0 \leq k_T \leq 1$ , corresponding to purely isotropic and purely tangential ejection, respectively. As a guide, we cite the nucleus of 9P/Tempel 1, which had  $0.005 \leq k_T \leq 0.04$  (Belton et al. 2011). We take  $P = 6$  hr, this being the median period of nine sub-kilometer nuclei as summarized by Kokotanekova et al. (2017). Assuming that the bulk of the outflow momentum is carried by the gas, we again set  $V_{\text{th}} = 480 \text{ m s}^{-1}$ .

Comet 2I spends  $\sim 0.6$  yr with  $r_H < 3$  au, where sublimation of water is strong enough to torque the nucleus. Setting  $\tau_s = 0.6$  yr in Equation (4) and using the parameters listed above, we find that a nucleus smaller than  $r_n \lesssim 0.3$  ( $k_T = 0.005$ ) to  $0.5$  km ( $k_T = 0.04$ ) could be spun up during the current solar flyby. This is comparable to the inferred size of 2I,  $0.2 \leq r_n \leq 0.5$  km, meaning that we should expect the nucleus spin to change, possibly by a large amount and conceivably enough to induce rotational breakup. Observers should be alert to this possibility when taking post-perihelion observations of the comet.

We briefly consider the implications of the discovery of 2I (at  $r_H = 3.0$  au) in the context of the number density of interstellar interlopers,  $N_1$ . Early estimates based on the detection of 1I alone gave  $N_1(r_n > 100 \text{ m}) \sim 0.1 \text{ au}^{-3}$  (Jewitt et al. 2017) and  $0.2 \text{ au}^{-3}$  (Do et al. 2018). At these densities we expect an average of  $\sim 10$ – $20$  ’Oumuamua scale or larger objects inside a 3 au radius sphere at any instant (the vast



majority of which are too distant and faint to be detected in ongoing sky surveys). If the number of interlopers is distributed as a differential power law,  $dN(r_n) \propto r_n^{-q} dr_n$ , with index  $q = 3$  to 4 (i.e., cumulative distribution  $N(r > r_n) = \int_{r_n}^{\infty} N(r_n) dr_n \propto r_n^{1-q} \propto r_n^{-2}$  to  $r_n^{-3}$ ), then the expected number of objects with  $r_n \geq 0.5$  km and  $r_H < 3$  au should fall in the range 0.8–0.08, respectively. Given these expected means and assuming Poisson statistics, the probabilities of there being a single 0.5 km object with  $r_H < 3$  au are 0.36 and 0.07, respectively. Therefore, the discovery of 2I is consistent with extrapolations based on 1I alone. It might be thought that the case is complicated by cometary activity, without which 2I would not have been discovered at small solar elongation (in late August a bare  $r_n = 0.5$  km nucleus would have had apparent magnitude  $V \sim 22.3$ , fainter than is reached by any near-Sun survey). However, even without activity, the apparent magnitude of a 0.5 km nucleus in the orbit of 2I rises to  $V \sim 20.7$  at perihelion, bright enough to be detected in several ongoing sky surveys (e.g., Catalina Sky Survey, Pan-STARRS). We conclude that, while 2I's early detection was certainly enabled by its cometary activity, the nucleus could have been detected later even if completely inert.

Finally, we consider the impact of interstellar bodies into the Earth. Meteor observations provide an observational constraint at small sizes. Specifically, survey observations set an upper limit to the flux of interstellar grains of mass  $> 2 \times 10^{-7}$  kg (radius  $> 0.5$  mm for  $\rho = 500$  kg m $^{-3}$ ) of  $F < 2 \times 10^{-4}$  km $^{-2}$  hr $^{-1}$  (Musci et al. 2012). (Detection of a 0.5 m scale interstellar impactor has been claimed in a preprint; Siraj & Loeb 2019.) The implied cumulative number density is then  $N_1(>0.5 \text{ mm}) = F/\Delta V$ , where we take  $\Delta V = 50$  km s $^{-1}$  as the nominal impact velocity. Substitution gives  $N_1(>0.5 \text{ mm}) \lesssim 4 \times 10^{15}$  au $^{-3}$ . By comparison with  $N_1(>100 \text{ m}) = 0.1\text{--}0.2$  au $^{-3}$ , we find that the size distribution of interstellar bodies between 0.5 mm and 100 m in radius can be represented as a differential power law having index  $q < 4$ . In such a distribution, the total mass is spread widely over a range of particle sizes, not concentrated in the smallest particles.

At large sizes, the rate of impact of  $r_n \gtrsim 100$  m interstellar bodies into Earth (radius  $R_{\oplus} = 6.4 \times 10^6$  m), neglecting gravitational focusing, is  $\tau_1^{-1} = N_1 \pi R_{\oplus}^2 \Delta V \sim (5 \text{ to } 10) \times 10^{-9}$  yr $^{-1}$ , corresponding to an impact interval 100–200 Myr. Over the age of the Earth, there have been  $\sim 25\text{--}50$  such impacts, most of a scale likely to generate airbursts. The total mass of interstellar material delivered is  $\lesssim 10^{-12} M_{\oplus}$  ( $1M_{\oplus} = 6.0 \times 10^{24}$  kg). In comparison, the terrestrial collision rate with (Sun orbiting) interplanetary debris larger than 100 m is  $\tau^{-1} \sim 2 \times 10^{-5}$  yr $^{-1}$  (Equation (3) of Brown et al. 2002) corresponding to a collision interval  $\tau = 5 \times 10^4$  yr. The ratio of the impact fluxes from interstellar to gravitationally bound projectiles is  $\tau_1/\tau \sim 10^{-4}$ , indicating the relative insignificance of the former.

#### 4. Summary

We used the *HST* to observe the newly discovered interstellar comet 2I/(2019 Q4) Borisov at the highest angular resolution. Three independent constraints show that the nucleus is a sub-kilometer body.

1. Measurements of the surface brightness profile provide the most robust (least model-dependent) constraint on the nucleus radius,  $r_n \leq 0.5$  km (albedo 0.04 assumed).

Substantially larger nuclei with this albedo would create a measurable excess in the central surface brightness profile that is not observed.

2. An empirical limit to the nongravitational acceleration of the comet sets a limit to the radius  $r_n > 0.2$  km (for density  $\rho = 500$  kg m $^{-3}$ ). No solution exists for nucleus density  $\rho < 25$  kg m $^{-3}$ , ruling out low-density fractal structure models as proposed elsewhere for 1I/'Oumuamua.
3. Gas production from comet Borisov matches that expected from full surface, equilibrium sublimation of a nucleus  $r_n = 0.4$  km in radius. However, this constraint is weak because the active fraction,  $f_A$ , is unmeasured; the nucleus could be larger if  $f_A < 1$ , or smaller if  $f_A > 1$ , as is possible if sublimation proceeds from volatile-rich grains in the coma.
4. The spin-up time for a  $r_n \leq 0.5$  km radius nucleus owing to outgassing torques is comparable to or less than the time spent by Borisov inside 3 au, where sublimation of water ice is nonnegligible. Therefore, we expect the spin state to change between the discovery epoch and the final observations in late 2020. Rotational disruption of the nucleus might also occur.
5. The interstellar differential size distribution from 0.5 mm to 100 m can be represented by a power law with index  $q < 4$ . Interstellar objects with  $r_n \gtrsim 0.1$  km strike Earth on average once every  $10^8$  to  $2 \times 10^8$  yr.

We thank Davide Farnocchia and Quanzhi Ye for discussions and Jing Li, Chien-Hsiu Lee, Amaya Moro-Martin, and the anonymous referee for comments on the manuscript. This work was supported under Space Telescope Science Institute program GO 16009. Y.K. and J.A. were supported by the European Research Council Starting grant 757390 ‘‘CAstRA.’’  
*Facility: HST.*

#### ORCID iDs

Man-To Hui  <https://orcid.org/0000-0001-9067-7477>  
Jessica Agarwal  <https://orcid.org/0000-0001-6608-1489>

#### References

- A’Hearn, M. F., Millis, R. C., Schleicher, D. O., et al. 1995, *Icar*, **118**, 223  
Bannister, M. T., Schwamb, M. E., Fraser, W. C., et al. 2017, *ApJL*, **851**, L38  
Belton, M. J. S., Meech, K. J., Chesley, S., et al. 2011, *Icar*, **213**, 345  
Bialy, S., & Loeb, A. 2018, *ApJL*, **868**, L1  
Bohren, C. F., & Huffman, D. R. 1983, *Absorption and Scattering of Light by Small Particles* (New York, Chichester, Brisbane, Toronto, Singapore: Wiley)  
Bolin, B. T., Lisse, C. M., Kasliwal, M. M., et al. 2019, arXiv:1910.14004  
Borisov, G. 2019, MPEC, 2019-R106, 1  
Brown, P., Spalding, R. E., ReVelle, D. O., et al. 2002, *Natur*, **420**, 294  
Do, A., Tucker, M. A., & Tonry, J. 2018, *ApJL*, **855**, L10  
Drahus, M., Guzik, P., Waniak, W., et al. 2018, *NatAs*, **2**, 407  
Fernández, Y. R., Kelley, M. S., Lamy, P. L., et al. 2013, *Icar*, **226**, 1138  
Fitzsimmons, A., Hainaut, O., Meech, K. J., et al. 2019, *ApJL*, **885**, L9  
Flekkøy, E. G., Luu, J., & Toussaint, R. 2019, *ApJL*, **885**, L41  
Groussin, O., Attree, N., Brouet, Y., et al. 2019, *SSRv*, **215**, 29  
Guzik, P., Drahus, M., Rusek, K., et al. 2019, *NatAs*, in press  
Hui, M.-T., & Li, J.-Y. 2018, *PASP*, **130**, 104501  
Jewitt, D. 1997, *EM&P*, **79**, 35  
Jewitt, D., Kim, Y., Luu, J., et al. 2019, *AJ*, **157**, 103  
Jewitt, D., & Luu, J. 2019, *ApJL*, **886**, L29  
Jewitt, D., Luu, J., Rajagopal, J., et al. 2017, *ApJL*, **850**, L36  
Kokotanekova, R., Snodgrass, C., Lacerda, P., et al. 2017, *MNRAS*, **471**, 2974  
Krist, J. E., Hook, R. N., & Stoehr, F. 2011, *Proc. SPIE*, **8127**, 81270J

Marsden, B., Sekanina, Z., & Yeomans, D. 1973, *AJ*, 78, 211  
McKay, A. J., Cochran, A. L., Dello Russo, N., et al. 2019, arXiv:1910.12785  
Meech, K. J., Weryk, R., Micheli, M., et al. 2017, *Natur*, 552, 378  
Micheli, M., Farnocchia, D., Meech, K., et al. 2018, *Natur*, 559, 223  
Moro-Martín, A. 2018, *ApJ*, 866, 131

Moro-Martín, A. 2019, *ApJL*, 872, L32  
Musci, R., Weryk, R. J., Brown, P., et al. 2012, *ApJ*, 745, 161  
Sekanina, Z. 2019, arXiv:1911.06271  
Siraj, A., & Loeb, A. 2019, arXiv:1904.07224  
Ye, Q., Kelley, M. S. P., Bolin, B. T., et al. 2019, arXiv:1911.05902